Wavelength-scale deformed microdisk lasers

Q. H. Song, Li Ge, J. Wiersig, J.-B. Shim, J. Unterhinninghofen, A. Eberspächer, W. Fang, G. S. Solomon, and Hui Cao

Phys. Rev. A **84**, 063843 — Published 22 December 2011

DOI: 10.1103/PhysRevA.84.063843

Wavelength-Scale Deformed Microdisk Lasers

Q. H. Song,[1,*] Li Ge,[2] J. Wiersig,[3] J.-B. Shim,[3] J. Unterhinninghofen,[3,†]
A. Eberspächer,[3] W. Fang,[4] G. S. Solomon,[4] A. D. Stone,[1] and Hui Cao[1]

[1]*Department of Applied Physics, Yale University, New Haven, CT 06520-8482, USA*
[2]*Department of Electrical Engineering,*
Princeton University, Princeton, New Jersey 08544
[3]*Institut für Theoretische Physik, Universität Magdeburg,*
Postfach 4120, D-39016 Magdeburg, Germany
[4]*Joint Quantum Institute, NIST and University of Maryland,*
Gaithersburg, Maryland 20899, USA

Abstract

We investigate lasing and output directionality of limaçon-shaped microdisk lasers of dimensions comparable to the emission wavelength. The far-field patterns are shown to differ between lasing modes, unlike in large cavities where lasing modes exhibit universal emission directionality determined by chaotic ray dynamics. Unidirectional emission is obtained for certain modes in the wavelength scale cavities. It results from weak coupling of nearly isotropic high-quality resonances to anisotropic low-quality resonances, combined with chiral symmetry-breaking of clockwise and counterclockwise propagating waves. The latter is described by an extended ray dynamics which includes the Goos-Hänchen shift and the Fresnel filtering. Mode hybridization and wave effects in open cavities make it possible to control the output properties of individual lasing modes in wavelength-scale lasers.

* Current address: National Key Laboratory of Tunable Laser Technology, Institute of Opto-Electronics, Harbin Institute of Technology, Harbin, 150080, China

† Current address: OEC AG, Lindwurmstr. 41, D-80337, München, Germany

I. INTRODUCTION

Optical microcavities are important photonic devices for confinement and control of light, and have triggered considerable research interests in past decades [1, 2]. Prominent examples are the whispering-gallery-mode (WGM) based microcavities such as microdisks [3], microrings [4], microspheres [5], microdroplets [6], and microtoroids [7]. In these cavities light is strongly confined by total internal reflection from the cavity boundary, resulting in a quality (Q) factor as high as 7×10^5 for microdisks [8], 6×10^7 for microtoroids [9], and 8×10^9 for microspheres [5]. The ultrahigh Q and largely in-plane emission make microdisks useful for diverse applications from ultralow-threshold lasers to single photon emitters and demonstrating solid state cavity quantum electrodynamics [1, 10, 11]. For wide bandgap semiconductors such as GaN and ZnO, microdisks are preferable over other cavity geometries such as vertical cavity surface emission micropillars due to technical difficulties in mirror fabrication [12]. However, due to the rotational symmetry of a circular cavity, light emission is isotropic in the far field and the efficiency of light collection is very low. To increase the collection efficiency, a tapered fiber or waveguide is often placed in close proximity of the cavity boundary to extract light [9, 13–16]. Nanoscale precision is needed in positioning the waveguide with respect to the cavity in order to obtain sufficient output while avoiding dramatic Q reduction. The vertical coupling between a waveguide and a microdisk [17, 18] can be well controlled to couple light efficiently. This scheme relies on wafer bonding and subsequent removal of a substrate, which is extremely difficult to implement for microdisks made of wide bandgap materials.

Shortly after realizing the first microdisk laser [3], Levi *et al.* demonstrated directional laser output by introducing a tab on its circumference [19]. Several types of defects such as a line [20, 21], an air hole [22], a notch [23] or a point scatterer [24] have been designed to obtain unidirectional output since then, but they introduce serious Q spoiling. Recently, output beams of divergence angle as small as several degrees have been obtained for high Q modes [25, 26] via a notch on the boundary of an elliptical cavity or a nano-scatterer in the evanescent wave zone outside a circular disk. To realize such design at optical frequency requires fine control of nanofabrication.

Another approach to obtain directional output while maintaining the high Q value is to smoothly deform the cavity shape to break the rotational symmetry [27, 28]. Such asym-

metric resonant cavities (ARCs) often have chaotic ray dynamics in most of the phase space [29]. When the cavity size is much larger than the wavelength, the emission directionality is usually predictable from the knowledge of the phase space dynamics, and in particular from the flow of the unstable manifolds of short unstable periodic orbits (UPOs) [30, 31]. This approach is robust, allowing the microcavities to be fabricated with standard photolithography that is suitable for mass production and large-scale integration. Directional emissions have been demonstrated with a number of ARCs [30–39]. Recently a very promising shape was shown to have unidirectional emission combined with relatively high Q factor [40]. The cavity boundary is defined by the limaçon of Pascal $\rho = R(1 + \epsilon \cos \phi)$, where ρ and ϕ are the radial coordinate and polar angle respectively. Although the intracavity ray dynamics is predominantly chaotic, high-Q scar modes are formed by wave localization on the UPOs with incident angles at the cavity boundary larger than the critical angle of reflection. The output directionality is universal for all the high-Q scar modes because the corresponding escape routes of rays are along the same unstable manifolds. Several experiments confirmed these predictions [41–44]. For example, we obtained a record high Q of 22000 from a 5 μm GaAs disk, and observed identical unidirectional output for all the lasing modes regardless of their wavelengths and intracavity mode structures. In these experiments, the cavity size is significantly larger than the wavelength of laser emission, and the ray dynamics dominates.

With rapid advances in nanophotonics and high density optical integration, there is much interest in developing nanoscale coherent light sources. Despite of recent progress in cavity size reduction, the in-plane output directionality of such devices has not been explored. Compared to the other two approaches mentioned, tailoring the cavity boundary is considered to be a more promising way of making ultrasmall laser cavities. However, the model explaining and predicting directional emission in the limaçon and other microcavity lasers is based on a universal flow of chaotic rays in phase space. It is expected to break down as the wavelength approaches the cavity size, where wave transport differs substantially from ray transport. It is therefore interesting to see if smoothly deformed *wavelength-scale* cavities can still achieve simultaneously unidirectional emission and high-Q factor.

As $kR \to 1$ ($k = 2\pi/\lambda$, where λ is the vacuum wavelength), the mode spacing becomes larger and the deformation from circular symmetry is effectively a weaker perturbation. One would expect high-Q modes (HQMs) to appear as smooth deformations of conventional whispering gallery (WG) modes of the circular disk, with relatively large angular momentum

and roughly isotropic emission. This expectation has been recently confirmed by calculations on "partial barrier" in phase space [45]. The lower-Q modes (LQMs) with smaller angular momentum will be more anisotropic, but these modes would not show up in the lasing spectrum because of their high thresholds. However, in recent experiments we observed lasing modes with unidirectional emission from wavelength-scale lasers, and found that it arises from the coupling of nearly isotropic HQMs to more directional LQMs [46].

In general, as two resonances approach each other, they may couple either strongly or weakly. In the case of weak coupling the frequencies of two modes cross while their Q-values anti-cross, and no "exchange of identity" takes place. For strong coupling the frequencies anti-cross but the Qs cross, and there is an "exchange of identity" [47–51]. The weak coupling scenario was exploited [22] to hybridize an isotropic HQM and a LQM to a resonance with a high quality factor and the directed far-field pattern of the LQM. This scheme was initially illustrated in a theoretical study of an annular cavity, a GaAs microdisk with a circular air hole [22]. The problem of this particular system is the coexistence of even and odd symmetry modes with different far-field patterns, which smears out the output directionality. We demonstrated experimentally this scheme works in a different system – wavelength-scale ARC lasers [46]. A detailed analysis will be presented in this article.

For wavelength-scale cavities, the ray model is expected to break down. However, it has been shown that the description using phase space distributions (in the following called "beams") rather than individual rays allows to capture certain wave effects. One is the "Goos-Hänchen" shift (GHS) [51–54], a lateral displacement of a beam total-internally reflected from a flat dielectric interface. Such a displacement is on the order of optical wavelength and originates from different phases accumulated by partial waves in a beam. The other is "Fresnel Filtering" (FF) [55, 56], a correction to the specular reflection and Snell's law of refraction of beams at a dielectric interface, due to their spread in transverse momentum beyond the critical angle. It has the effect of deflecting the reflected beam away from the normal of the interface. Both have been included as the first-order wave correction in recent attempts to amend the ray dynamics [51–54]. In this work we are able to explain the output directionality of the LQMs in the wavelength-scale ARC with the extended ray dynamics.

The paper is organized as follows. Section II describes sample fabrication and characterization. In Sec. III, experimental results of wavelength-scale ARC lasers are presented.

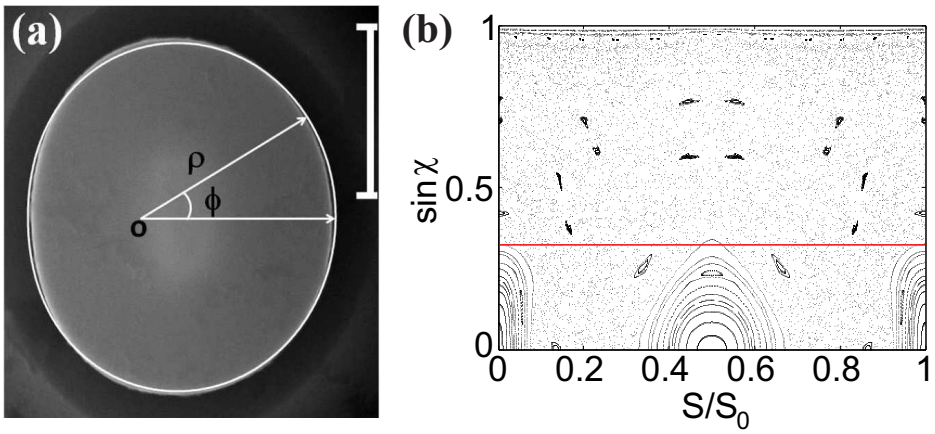

FIG. 1. (a) Top-view SEM image of a GaAs disk. The scale bar indicates 1 μm. The cavity boundary is fitted in polar coordinates by Eq. (1) (white curve). (b) Poincaré SOS showing ray trajectories in the corresponding closed billiard. S is the arclength coordinate and χ is the angle of incidence at the boundary. S_0 is the perimeter of cavity. The ray dynamics is predominately chaotic.

Section IV contains numerical simulations based on wave optics and extended ray dynamics. Finally we conclude in Sec. V.

II. SAMPLE FABRICATION AND RAY SIMULATION

We fabricated GaAs microdisk lasers with embedded InAs quantum dots (QDs) as the gain media. The sample is grown on GaAs substrate by molecular beam epitaxy. The layer structure consists of 1000 nm $Al_{0.68}Ga_{0.32}As$ and 265 nm GaAs. Inside the GaAs layer there are six monolayers of InAs QDs equally spaced by 25 nm GaAs barriers. Standard photolithography is used to define limaçon-shaped microdisks with $R = 3.75\,\mu$m and $\epsilon = 0.43$. Next GaAs and $Al_{0.68}Ga_{0.32}As$ are etched nonselectively in a mixture of $HBr:H_2O_2:H_2O$ with the ratio 4:1:25 [57]. The etching is nearly isotropic, and the radius of microdisk decreases with increasing the etching time [58]. Finally 2.5% diluted HF is used to etch the $Al_{0.68}Ga_{0.32}As$ and form a pedestal underneath the GaAs disk [58]. Figure 1(a) shows the top-view scanning electron microscope (SEM) image of a fabricated disk. Its shape is slightly distorted from the limaçon by the wet etching and a fitting of its boundary gives

$$\rho(\phi) = R(1 + \epsilon\cos\phi)(1 - \epsilon_1\cos 2\phi) + d\ , \tag{1}$$

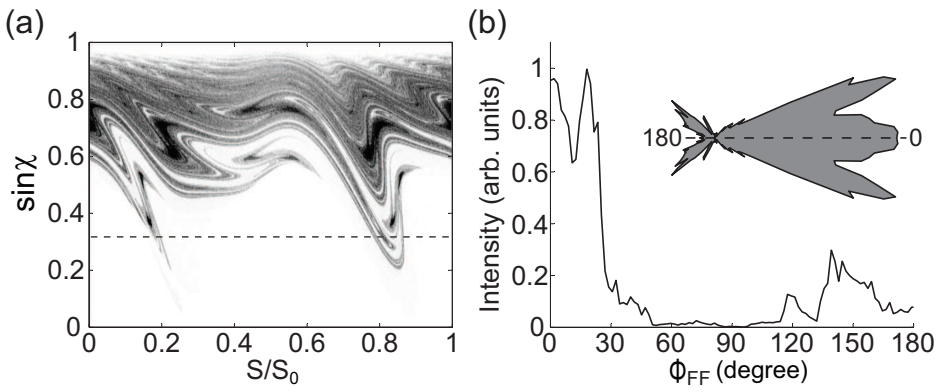

FIG. 2. (a) Fresnel weighted ray tracing in a dielectric disk (refractive index = 3.13) whose boundary is given by Eq. (1) showing the rays escape along the unstable manifolds to the leaky area ($\sin\chi < \sin\chi_c$). (b) Far-field emission pattern in the linear scale predicted by ray tracing. The inset is the angular distribution of far-field intensity.

where $R = 890\,\mathrm{nm}$, $\epsilon = 0.28$, $\epsilon_1 = 0.06$, and $d = 60\,\mathrm{nm}$. The cavity size is much smaller than that in the previous reports [41–44]. As shown in Fig. 1(a), the angle ϕ uniquely specifies a point on the boundary, but to avoid confusion, below we use ϕ_{FF} to designate far-field directions, and the arc-length S, measured from the boundary point on the positive x-axis and normalized to the perimeter, to specify points on the boundary.

Although the fabricated cavity shape slightly deviates from the limaçon, the classical ray dynamics is very similar. A two-dimensional (2D) phase space representation, the so-called Poincaré surface of section (SOS), is shown in Fig. 1(b). Every time the trajectory hits the cavity boundary, its position S and tangential momentum $\sin\chi$ (the angle of incidence χ is measured from the boundary normal) is recorded. We first consider a closed cavity with perfect reflection of light from the boundary. Similar to the case of limaçon cavity, the ray dynamics is predominantly chaotic. Because the ray cannot escape from the boundary, a typical trajectory could explore almost the entire phase space in a random fashion. In addition to the chaotic orbits, there are stable periodic orbits that correspond to a few tiny islands in SOS and two big islands near $\sin\chi \simeq 0$. Although invisible, there are numerous unstable periodic orbits in the chaotic sea. WG trajectories are confined in the narrow band with $|\sin\chi| > 0.99$.

Next we performed the ray tracing simulation in an open cavity from which light can escape via refraction at the boundary. For the lowest order transverse electric (TE) waveguide

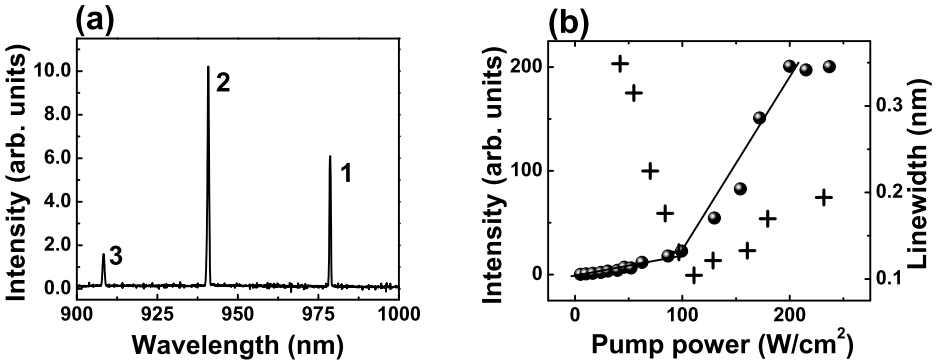

FIG. 3. (a) Measured emission spectrum at the incident pump intensity of 191 W/cm^2. It consists of three peaks labeled 1, 2, and 3. (b) Emission intensity (circles) and linewidth (crosses) of peak 3 in (a) as a function of pump intensity in the linear scale. A clear threshold behavior is seen at $\sim 100\,\mathrm{W/cm^2}$. The linewidth first decreases and then increases at higher pump due to the hot carrier effect.

mode in the GaAs layer, we computed the effective index of refraction $n_{eff} = 3.13$. Initially rays with identical amplitudes are uniformly distributed in the phase space above the critical line. As they propagate inside the cavity, their amplitudes are reduced according to the Fresnel law upon each reflection from the boundary. Tracing of one ray is stopped after its amplitude falls below a small threshold value. Figure 2(a) shows the distribution of optical ray amplitudes obtained by tracing 20,000 rays propagating counterclockwise (CCW) inside the cavity. It reveals that the rays diffuse along the unstable manifolds toward the leaky region of $\chi < \chi_c = \arcsin(1/n_{eff})$, where χ_c the critical angle for total internal reflection from the disk boundary. The far field pattern is shown in Fig. 2(b). The directed flow of rays in the phase space produces an output beam in the forward direction ($\phi_{FF} = 0$).

We note that classical ray model, which predicts highly directional emission, holds in the semiclassical region (large kR). It is expected to break down in wavelength-scale cavities, where the value of kR approaches one. Can directional emission still be obtained from such small cavities? This question will be addressed first experimentally in the next section.

III. LASING EXPERIMENT

In our lasing experiment, the sample is mounted in a liquid Helium cryostat with the substrate temperature kept at 10 K, and optically pumped by a mode-locked Ti:Sapphire

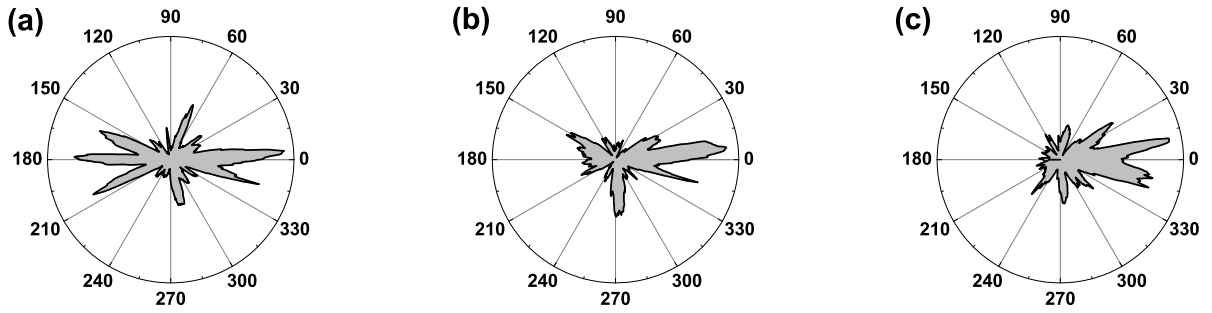

FIG. 4. (a), (b), and (c) are the measured far-field patterns in degree for the lasing modes 1, 2, and 3 labeled in Fig 3(a). The incident pump intensity is kept at 191 W/cm^2.

laser (pulse width 200 fs, 76 MHz repetition rate). The pump wavelength is 790 nm. A long-working-distance objective lens is used to focus the pump beam normally to a single disk from the top and collect the emission reversely. Time-integrated spectra are taken by a spectrometer with a cooled CCD array detector. Only the high-Q modes of frequencies within the gain spectrum manage to lase. The InAs QDs have an inhomogeneously-broadened gain spectrum of width ~ 80 nm. Thus we are able to observe several lasing modes despite the large mode spacing in the small disk. Figure 3(a) is an emission spectrum that consists of three peaks at vacuum wavelengths $\lambda = 908$ nm, 942 nm, and 978 nm, corresponding to three consecutive cavity resonances labeled 1-3. Figure 3(b) shows the pump-dependence of the emission intensity of the mode at $\lambda = 908$ nm. When the pump intensity is higher than ~ 100 W/cm^2, the emission intensity increases dramatically, displaying a threshold behavior at ~ 100 W/cm^2. We also measured the linewidth of this mode as a function of pump intensity, as seen in Fig. 3(b). It first decreases rapidly to 0.1 nm, and then gradually increases, mostly due to temporal shift of lasing frequency with short pulse pumping [59]. In our time-integrated measurement of the lasing spectrum, the transient frequency shift results in a broadening of the lasing line. Such broadening increases with the hot carrier density and becomes dominant at high pumping level.

To measure the far-field pattern of laser emission, we fabricated a large ring structure around each disk. The in-plane emission from the disk edge propagates to the ring and is scattered out of the plane. The scattered light pattern is imaged by the objective lens to a CCD camera. Since the ring radius exceeds $4R^2/\lambda$, the scattered light intensity along the ring reflects the far-field emission pattern. Bandpass filters have been placed in front of the CCD

camera to measure the far-field patterns of three lasing modes in Fig. 3(a). The measured far-field patterns are presented in Fig. 4. All the three lasing modes have significantly different far-field patterns. Mode 3 has output predominantly in the forward direction ($\phi_{FF} = 0°$), while mode 1 displays bidirectional emission in both forward and backward ($\phi_{FF} = 180°$) directions. Mode 2 is intermediate between 1 and 3. This phenomenon is distinct from that of larger cavities which have identical unidirectional emission patterns for all lasing modes. It indicates the breakdown of classical ray dynamics in the wavelength scale cavities. The failure of the ray model in wavelength-scale deformed microdisk lasers is expected; this statistical model is more appropriate for multimode lasing in the limit of short wavelength ($kR \gg 1$). However the persistence of unidirectional emission to such small scales (mode 3) is surprising.

IV. WAVE SIMULATION AND MODIFIED RAY DYNAMICS

To explain the experimental observations, we solved the electromagnetic wave equations for the cavity resonances after extracting the actual disk shape and dimension from the SEM images. Three numerical methods were used: a finite-difference time-domain (FDTD) algorithm [41], the scattering matrix approach [56], and boundary element method [60], and they give consistent results. We find a set of HQMs with constant frequency spacing and similar spatial profile; in most cases these modes look like WG modes, with vanishing intensity towards the disk center. However, their Q values exhibit an unusual non-monotonic variation with frequency, reaching a local minimum at $kR \sim 7.1$ [Fig. 5(a)]. In addition we find a LQM series in the same frequency range, the relevance of which will be discussed below.

To characterize the directionality of the output we use the measure

$$U = \int I(\phi_{FF}) \cos\phi_{FF} d\phi_{FF} / \int I(\phi_{FF}) d\phi_{FF}, \tag{2}$$

where $I(\phi_{FF})$ represents the angular distribution of far-field intensity. $U = 0$ corresponds to isotropic or bidirectional emission, whereas positive (negative) U corresponds to emission primarily towards $\phi_{FF} = 0°(180°)$. We find that as kR decreases from 10 to 5.5, the value of U for the HQM series first increases from approximately 0 to 0.6 and then decreases to 0, while the U of the LQMs stays nearly constant around 0.4. [Fig. 5(b)]. Figure 6 shows

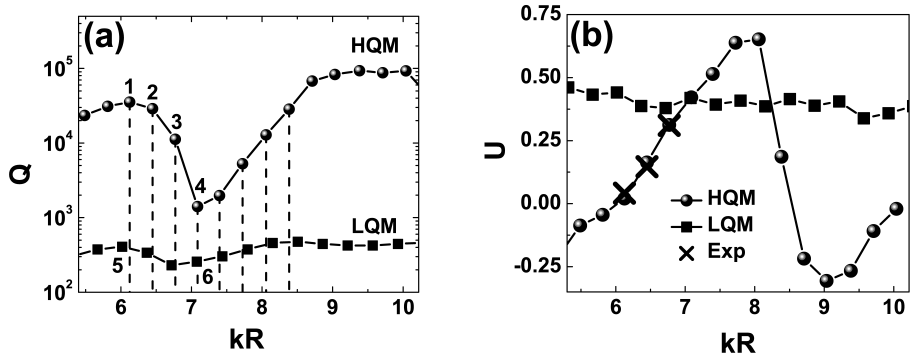

FIG. 5. (a) Calculated Q values for the HQMs (dots) and the LQMs (squares). Modes marked 1, 2, and 3 correspond to the three lasing modes in Fig. 3(a). (b) Directionality U of the HQMs and LQMs vs. kR. Here $k = 2\pi/\lambda$ is the wavevector. Crosses are U values of the three lasing modes in Fig. 3(a).

the calculated far-field patterns of modes labeled 1-6 in Fig. 5(a). The calculated far-field patterns confirm a transition from bidirectional emission to unidirectional emission, and back to bidirectional emission for the HQMs. The LQMs display similar far-field patterns as kR varies, and they all emit predominantly in the forward direction. Our lasing experiment however cannot detect the lowest Q mode of the HQM series [labeled 4 in Fig. 5(a)] or the LQMs, because they do not lase, instead the three modes it measures [Fig. 3(a)] are the HQMs on the low kR (long wavelength) side of the Q dip and labeled 1, 2 and 3 in Fig. 5(a). The calculated angular distributions of far-field intensities of modes 1-3 resemble the measured ones, which change from bi-directional to unidirectional emission. The values of U computed from the measured far-field patterns of three lasing modes, also plotted in Fig. 5(b), agree well with the numerical-simulated values.

The maximum of U for the HMQ series almost coincides with the minimum of Q. It suggests the dip in Q is associated with the unidirectional emission; we therefore analyze the lowest Q and highest Q modes on the long wavelength side [1 and 4 in Fig 5(a)] for a clue to the mechanism of the unidirectional emission. The intensity plots for these two modes in Fig. 7 (a) and (c) show that while mode 1 is a smooth deformation of a WG mode with angular momentum quantum number $m = 16$, mode 4 appears to be a superposition of a similar WG mode and a much lower angular momentum mode with significant intensity away from the cavity boundary.

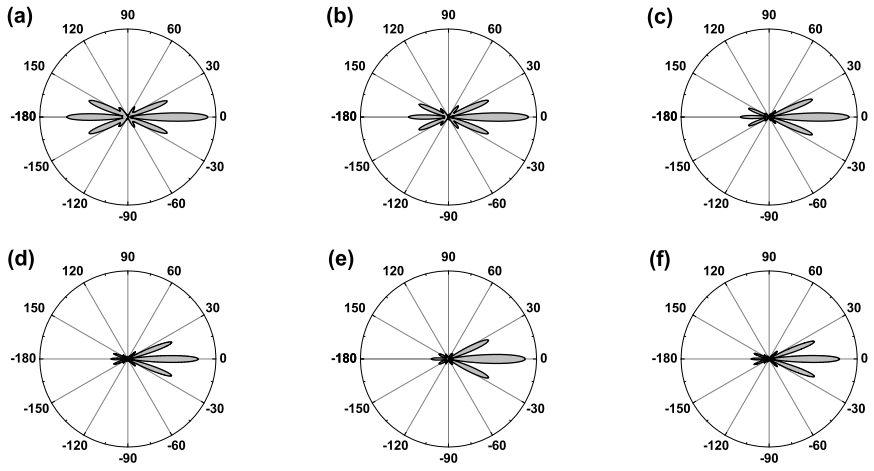

FIG. 6. (a)-(f) are the calculated far field patterns in degree of the modes 1-6 labeled in Fig. 5(a), respectively.

The effect of this superposition in mode 4 is most clearly seen by taking the photon wavefunction (field distribution) and performing the Husimi projection onto the SOS [61]. For mode 1 the Husimi function (see Fig.7 (b)) has four maxima at specific locations on the boundary and specific ray angles of incidence corresponding to the "diamond orbit" which is superposed on the spatial intensity profile in Fig. 7 (a). The Husimi function below the critical angle has the largest amplitude near the bounce points labeled ii, iv, where the curvatures of boundary are the highest among the four bounce points and most of the emission occurs. Here, the emission is therefore due to tunneling and not due to the unstable manifold. Note that the SOS for mode 1 (Fig. 7 (b)) has approximate symmetry about $S = 0, 0.5$. Such a Husimi function must lead to approximately equal emission into the forward and backward quadrants as we find for this mode. The small residual symmetry breaking arises from the relatively small distortion of the diamond orbit from reflection symmetry around the vertical axis of the cavity. In contrast, the Husimi function for mode 4 (Fig. 7 (d)) shows a large symmetry breaking around $S = 0.5$ which leads to the unidirectional emission primarily from region around $S = 0.8$ on the boundary in the $\phi_{FF} = 0$ direction in agreement with the unstable manifold in Fig. 2. Due to the symmetry, $H(S, \sin\chi) = H(1 - S, -\sin\chi)$, of the Husimi function, we only display the upper half ($\sin\chi > 0$) portion of the SOS corresponding to CCW circulating rays; the Husimi function in the lower half corresponding to clockwise (CW) circulating rays indicates strong emission

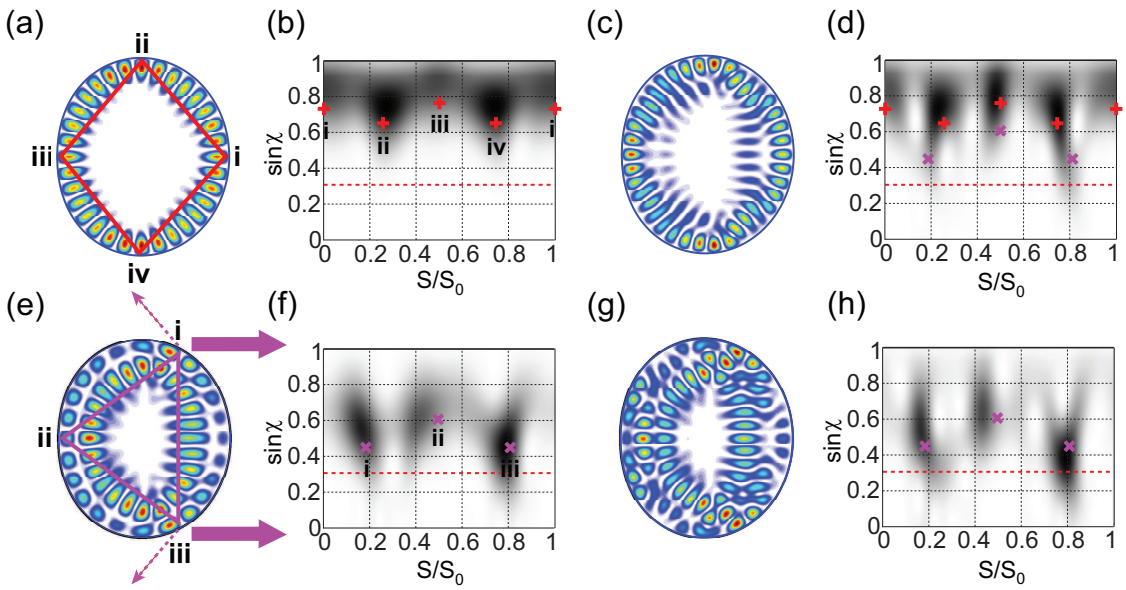

FIG. 7. (Color online) (a), (c), (e), (g) and (b), (d), (f), (h) are the spatial profiles of magnetic field intensity and Husimi functions of the cavity modes labeled 1, 4, 5 and 6 in Fig. 5(a), respectively.

from $S = 0.2$ but of the oppositely circulating rays, leading to far-field emission in the $\phi_{FF} = 0$ direction as well.

It is not easy to tell from the Husimi functions why mode 4 is much leakier than mode 1, however this becomes evident from considering modes 5 and 6 of the LQM series also shown in Fig. 5(a). This mode series has Husimi functions well localized on a three-bounce periodic orbit drawn on the spatial intensity distribution of mode 5 in Fig. 7 (e). Since this orbit has two bounce points (labeled i and iii) much closer to the critical angle, this mode series has much lower Q than the HQM series based on the diamond orbit, and does not lase experimentally. This is consistent with our expectation that the more directional modes would not appear in the lasing spectrum.

The two series of HQMs and LQMs have different frequency spacing and thus it is possible to have particular pairs of modes (one from each series) that are nearly degenerate in their frequencies. This is exactly what happens for the modes 4 and 6 in Fig. 5(a). The HQM and LQM become weakly coupled, as their frequencies cross and Qs anti-cross in Fig. 5(a). The spatial intensity plots in Fig. 7 (c) reveal that mode 4 is a mixture of modes 1 and 5; this is clear for mode 6 (see Fig.7(g)) as well, which has a larger component of the leakier mode 5 and hence lower Q. Moreover, the phase space structure of modes 4 and 6

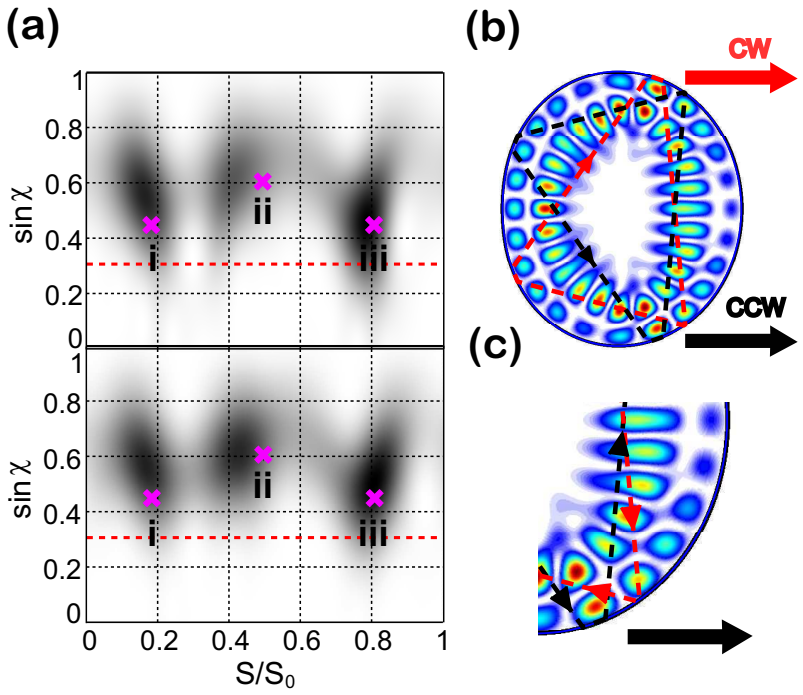

FIG. 8. (Color online) (a) Husimi projections of incident (top) and emergent (bottom) waves for mode 5. (b,c) CW and CCW pseudo-orbits extracted from the actual bouncing points in the Husimi distributions in (a).

(Husimi functions in Fig. 7 (f) and (h)) are almost the same near and below the critical line. Consequently, their far-field emission patterns are nearly identical. These data confirm that the modes are coupled and the output is dominated by the LQM component. Thus the violation of our expectation that high-Q modes would be approximately isotropic emitters arises from the weak coupling of an high-Q mode to a directional low-Q mode, which does not strongly degrade the Q but enables substantially directional output. While mode 4 is the most hybridized (and therefore too low Q to lase), the mode coupling for the experimentally observed mode 3 is sufficient to obtain directional emission. Its Q exceeds 10,000, high enough to lase with modest pumping.

We note that the coupling discussed above is the linear coupling of two resonant modes near a frequency crossing, not the non-linear coupling of lasing modes due to spectral hole-burning, which is negligible in our device due to the inhomogeneous gain broadening.

A final intriguing question is how to explain the broken symmetry of emission of the LQM series based on the triangle orbit. The orbit itself has symmetric bounce points (labeled i and iii in the spatial intensity plot of mode 5 in Fig. 7 (e)) which are at lower incidence

angle than bounce ii. Hence most of the emission occurs at bounces i and iii. A ray can traverse the triangle either CW or CCW, and by symmetry should emit at each point into the forward *and* backward directions. If this symmetry were obeyed by the photon "wavefunction" the unidirectionality would be lost; but the Husimi function of mode 5 in Fig. 7 (f) describing CCW rays ($\sin\chi > 0$) violates this symmetry and is indeed leakier at bounce iii than bounce i. The Husimi function for CW rays ($\sin\chi < 0$) has the opposite asymmetry and is leakier at point i, leading to the unidirectional emission.

This symmetry breaking can only come from the openness of the system, which distinguishes incident and reflected (emergent) rays. A qualitative explanation for it can be given by the two wave effects GHS and FF as introduced in Sec. I. The CW and CCW components behave essentially like trapped beams and "violate" ray dynamics due to these two effects. One can capture this effect semi-quantitatively with a modified ray dynamics in which the incident ray is translated along the boundary in the direction of motion according to the "Goos-Hänchen" shift law, before emerging at an angle of reflection greater than the angle of incidence due to the FF effect [51–54].

As was pointed out in Ref. [53], the extended ray dynamics including GHS and FF violates the chiral symmetry of the periodic orbits; a periodic orbit such as the triangle will now break into two distinct CW and CCW periodic pseudo-orbits. To confirm these two effects, we have analyzed the incident and emergent Husimi functions of mode 5 [61]. The crosses in Fig. 8(a) represent the bouncing points of the original symmetric triangle orbit. It is evident from Fig. 8(a) that the Husimi intensity maxima deviate from the classical ray prediction. The lateral shift (in S/S_0) between the maxima of incident and emergent Husimi intensities at the same bouncing point originates from the GHS, and the vertical shift (in $\sin\chi$) from the FF [52]. By extracting the location of each bouncing point from the intensity maxima in the Husimi distributions, we plot in Fig. 8(b) the CW and CCW pseudo-orbits that compose mode 5. The CCW orbit has a smaller angle of incidence at bounce iii than does the CW orbit, leading to unidirectional forward emission dominated by the CCW beam [Fig. 8(c)]. The corresponding effect occurs for the CW orbit near bounce i, so it dominates the emission, again in forward direction.

The conclusions drawn from Fig. 8 are confirmed independently by direct calculations based on the extended ray dynamics including the GHS and FF effects [51, 54]. Fig. 9 shows the period-3 orbits corresponding to the mode in Fig. 8(c). In the case of CCW (CW)

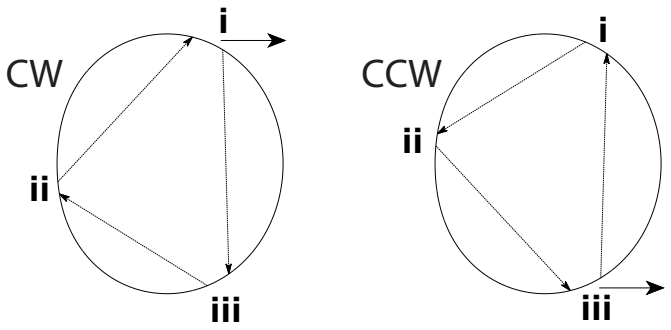

FIG. 9. Expected light emission pattern from CW and CCW rays for the asymmetric period-3 orbits of the extended ray dynamics. Both CW and CCW rays emit in the forward direction.

motion the angle of incidence is smallest at bounce point iii (i) leading to the strongest emission there. In both cases the emitted rays emanate in the same direction leading to a unidirectional output.

V. DISCUSSION AND CONCLUSION

In principle unidirectional emission can also be obtained via strong coupling between the HQM and LQM. However, the hybrid modes formed by strong coupling are mixtures of HQM and LQM with nearly 1:1 ratio, thus Q-spoiling is severe for the HQM and prohibits lasing experimentally. We also note that the mode coupling (weak or strong) does not modify the vertical (out of disk plane) divergence of far-field emission, as both HQM and LQM are confined vertically in the fundamental waveguide mode.

Although our study is focused on GaAs disks of specific shape, we find from our numerical simulation that relatively high-Q modes with unidirectional emission exist over wide ranges of cavity refractive index and shape deformation. As an example, Fig. 10(a) plots the U of the HQM at $kR \sim 7.4$ in Fig. 5(a). Its output remains unidirectional as the refractive index varies from 2 and 4. Hence, it is possible to obtain unidirectional emission from the wavelength-scale disk lasers made of nitride materials (see Fig. 10 (b)), where other cavity designs such as vertical-cavity surface-emitting laser (VCSEL) face severe challenges in mirror fabrications. Our numerical simulation also shows that unidirectional output can be obtained over a broad range of cavity shape deformation ($0.2 \leq \epsilon \leq 0.5$). For $\epsilon < 0.2$ the unidirectionality is lost, because the cavity approaches a circular disk.

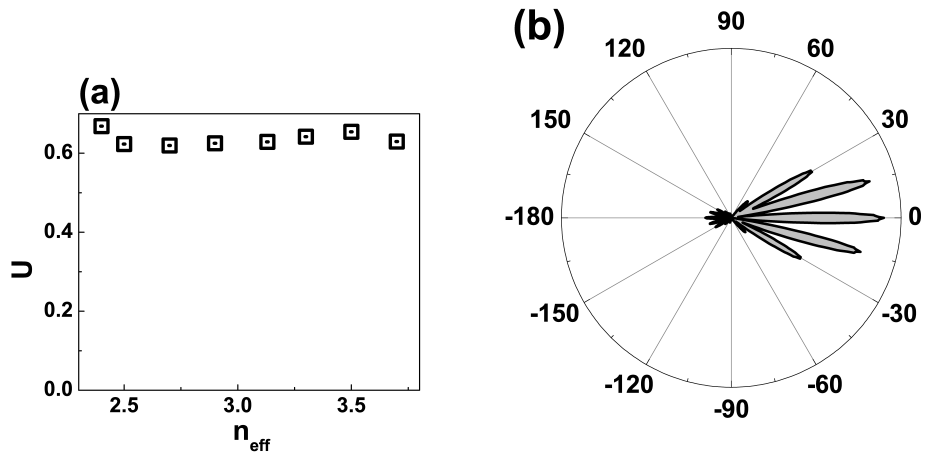

FIG. 10. (a) Output directionality U of the mode at $kR \sim 7.4$ in Fig. (5)(a) as a function of the refractive index n_{eff}. The cavity shape is described by Eq.1. (b) Calculated far-field pattern at $n_{eff} = 2.4$.

In summary, we have demonstrated directional outputs from an ARC laser with dimension comparable to the emission wavelength. This violates the expectation that in the regime of $kR < 10$ high-Q modes would have approximately isotropic emission but is explained by weak coupling of such modes to directional low-Q modes. The chiral symmetry breaking of clockwise and counter clockwise propagating waves in low-Q scar resonances can be described by an extended ray dynamics which includes the Goos-Hänchen shift and the Fresnel filtering. This is a new mechanism for generating directional emission in small cavities, distinct from the unstable manifold mechanism for universal directionality in larger cavities. Analysis of the Husimi projections of the modes and relating them to periodic orbits is a useful tool for understanding the properties of the lasing modes, and may be used to optimize the Q-values and output properties. Numerical simulations indicate that similar behaviors occur for a wide range of cavity deformation and the refractive index around their values in our experiment, making our design potentially useful for GaN lasers at blue and UV wavelengths as well.

This work is supported partly by NIST under the Grant No. 70NANB6H6162, by NSF under the Grant Nos. DMR-0808937 and DMR-0908437, and by the DFG research group

760.

[1] *Optical Microcavities*, K. J. Vahala, Ed., Advanced Series in Applied Physics, (World Scientific, 2004).

[2] K. J. Vahala, *Nature* **424**, 839 (2003).

[3] S. L. McCall *et al.*, *Appl. Phys. Lett.* **60**, 289 (1992).

[4] J. P. Zhang *et al.*, *Phys. Rev. Lett.* **75**,2678 (1995).

[5] M. L. Gorodetsky, A. A. Savchenkov, and V. S. lchenko, *Opt. Lett.* **21**, 453 (1996).

[6] S. X. Qian, J. B. Snow, H. M. Tzeng, and R. K. Chang, *Science* **231**, 486 (1986).

[7] D. K. Armani, T. J. Kippenberg, S. M. Spillane, and K. J. Vahala, *Nature (London)* **421**, 925 (2003).

[8] C. P. Michael *et al.*, *Appl. Phys. Lett.* **90**, 051108 (2007).

[9] T. J. Kippenberg, J. Kalkman, A. Polman, and K. J. Vahala, *Phys. Rev. A* **74**, 051802(R) (2006).

[10] E. Peter *et al.*, *Phys. Rev. Lett.* **95**, 067401 (2005).

[11] M. Fujita *et al.*, *Electronics Lett.* **36**, 790, (2000).

[12] H. Lohmeyer *et al.*, *Eur. Phys. J. B* **48**, 291 (2005).

[13] K. Srinivasan and O. Painter, *Nature* **450**, 862 (2007).

[14] S. J. Choi, K. Djordjev, S. J. Choi, and P. D. Dapkus, *IEEE Photon. Technol. Lett.* **15** 1330-1332 (2003).

[15] F. Ou *et al.*, *Opt. Lett.* **35**, 1722 (2010).

[16] J. P. Zhang *et al.*, *IEEE Photon. Technol. Lett.*, **8**, 968 (1996).

[17] D. V. Tishinin, P. D. Dapkus, A. E. Bond, I. Kim, C. K. Lin, and J. O'Brien, *IEEE photon. technol. lett.* **11**, 1003 (1999).

[18] S. J. Choi *et al.*, *IEEE Photon. Technol. Lett.* **16**, 828 (2004).

[19] A. F. J. Levi *et al.*, *Appl. Phys. Lett.* **62**, 561 (1993).

[20] V. M. Apalkov and M. E. Raikh, *Phys .REv. B* **70**, 195317 (2004).

[21] A. Tulek and Z. V. Vardeny, *Appl. Phys. Lett.* **90**, 161106 (2007).

[22] J. Wiersig and M. Hentschel, *Phys. Rev. A* **73**, 031802 (2006).

[23] S. V. Boriskina, T. M. Benson, P. D. Sewell, and A. I. Nosich, *IEEE J. Sel. Top. Quant.*

Electron. **12**, 1175 (2006).

[24] C. P. Dettmann, G. V. Morozov, M. Sieber, and H. Waalkens, *Europhys. Lett.* **82**, 34002 (2008).

[25] Q. J. Wang *et al.*, *Proc. Natl. Acad. Sci. USA* **107**, 22407 (2010).

[26] Q. H. Song and H. Cao, *Opt. Lett.* **36**, 103 (2011).

[27] J. U. Nöckel, and A. D. Stone, G. Chen, H. L. Grossman, R. K. Chang, *Opt. Lett.* **21**, 1609 (1996).

[28] J. U. Nöckel, and A. D. Stone, *Nature* **385**, 45 (1997).

[29] A. D. Stone, *Physica Scripta* **T90**, 248-262 (2001).

[30] H. G. L. Schwefel *et al.*, *J. Opt. Soc. Am. B* **21**, 923 (2004).

[31] S. -B. Lee *et al.*, *Phys. Rev. A* **75**, 011802(R) (2007).

[32] C. Gmachl *et al.*, *Science* **280**, 1556 (1998).

[33] T. Fukushima *et al.*, *Opt. Lett.* **27**. 1430 (2002).

[34] G. D. Chern *et al.*, *Appl. Phys. Lett.* **83**, 1710-1712 (2003).

[35] T. Harayama, T. Fukushima, S. Sunada, K. S. Ikeda, *Phys. Rev. Lett.* **91**, 073903 (2003).

[36] Y. Baryshnikov, P. Heider, W. Parz, and V. Zharnitsky, *Phys. Rev. Lett.* **93**, 133902 (2004).

[37] M. Lebental, J. S. Lauret, R. Hierle, and J. Zyss, *Appl. Phys. Lett.* **88**, 031108 (2006).

[38] J. W. Ryu, S. Y. Lee, C. M. Kim, and Y. J. Park, *Phys. Rev. E.* **73**, 036207 (2006).

[39] J. Gao *et al.*, *Appl. Phys. Lett.* **91**, 181101 (2007).

[40] J. Wiersig and M. Hentschel, *Phys. Rev. Lett.* **100**, 033901 (2008).

[41] Q. H. Song *et al.*, *Phys. Rev. A* **80**, 041807(R) (2009).

[42] C. L. Yan *et al.*, *Appl. Phys. Lett.* **94**, 215101 (2009).

[43] S. Shinohara, M. Hentschel, J. Wiersig, T. Sasaki, T. Harayama, *Phys. Rev. A* **80**, 031801(R) (2009).

[44] C. H. Yi *et al.*, M. W. Kim, and C. M. Kim, *Appl. Phys. Lett.* **95**, 141107 (2009).

[45] J.-B. Shim, and J. Wiersig, Submitted to *Phys. Rev. A*.

[46] Q. H. Song *et al.*, *Phys. Rev. Lett.* **105**, 103902 (2010).

[47] S. B. Lee *et al.*, *Phys. Rev. Lett.* **103**, 134101 (2009).

[48] J. Wiersig, *Phys. Rev. Lett.* **97**, 253901 (2006).

[49] S. B. Lee *et al.*, *Phys. Rev. A* **80**, 011802(R) (2009).

[50] Q. H. Song and H. Cao, *Phys. Rev. Lett.* **105**, 053902 (2010).

[51] J. Unterhinninghofen, J. Wiersig, and M. Hentschel, *Phys. Rev. E* **78**, 016201 (2008).

[52] H. Schomerus and M. Hentschel, *Phys. Rev. Lett.* **96**, 243903 (2006).

[53] E. G. Altmann, G. Del Magno, and M. Hentschel, *Europhys. Lett.* **84**, 10008, (2008).

[54] J. Unterhinninghofen and J. Wiersig, *Phys. Rev. E* **82**, 026202 (2010).

[55] H. E. Türeci and A. D. Stone, *Opt. Lett.* **27**, 7, (2002).

[56] H. E. Türeci, H. G. L Schwefel, P. Jacquod, and A. D. Stone, Chapter 2, *Progress in Optics* **47**, E. Wolf ed., Elsevier, 2005.

[57] B. Gayral *et al.*, *Appl. Phys. Lett.* **75** 1908 (1999).

[58] Q. H. Song, H. Cao, S. T. Ho, and G. S. Solomon, *Appl. Phys. Lett.* **94**, 061109 (2009).

[59] G. Pompe *et al.*, *Phys. Stat. Sol. (b)*, **188**, 175 (1995).

[60] J. Wiersig, *J. Opt. A: Pure Appl. Opt.* **5**, 53 (2003).

[61] M. Hentschel, H. Schomerus, and R. Schubert, *Europhys. Lett.* **62**, 636 (2003).